OBSERVATIONAL CONSTRAINTS ON THE DIFFUSION OF COSMIC-RAY ELECTRONS IN SPIRAL GALAXIES

K. A. MARSH AND G. HELOU

Infrared Processing and Analysis Center, California Institute of Technology 100-22, Pasadena, CA 91125;
kam@ipac.caltech.edu, gxh@ipac.caltech.edu

ABSTRACT

We present quantitative tests of the "smearing" model which relates radio and infrared images of spiral galaxies. We test whether the radio image appears as a smeared version of the infrared image in 24 spirals and one irregular, using 20 cm radio images and 60 μm infrared images processed to the same resolution of $\lesssim 1'$. Previous work by Bicay & Helou, assuming circularly symmetric, exponentially profiled disks, suggested that the smearing function is best approximated by an exponential radial profile. Our detailed assessment of the shape and size of the smearing function is free of those assumptions. We used two different approaches: (1) parameterized fits to exponential and Gaussian functions, each either circularly symmetric or elongated along the disk's tilt axis, and (2) direct estimation of the form of the kernel by deconvolution of the radio image against the infrared image. We conclude that:

1. The radio images are indeed reproduced to reasonable accuracy by smearing the infrared images with positive-valued kernels with model-error residuals $\leq 10\%$ of the local radio intensity over an intensity range of almost 2 orders of magnitude.

2. Most estimated smearing scales are smaller than 2 kpc and are typically 50% smaller than those reported by Bicay & Helou. This discrepancy is most likely due to the specific infrared intensity distribution assumed by Bicay & Helou.

3. The discrimination between exponential and Gaussian smearing kernels is marginal in most cases: above the 90% confidence level, only four galaxies are better fit by exponential kernels, and none is better fit by a Gaussian. There is also no improvement in the goodness of fit if we use direct deconvolution rather than parametric Gaussian or exponential fitting.

4. There is no evidence for a change of shape of the smearing kernel from one quadrant of the galaxy disk to another. The smearing is therefore unlikely to be elongated in the radial direction.

5. For some but not all galaxies inclined to the line of sight by 45° or more, the smearing function is significantly elongated parallel to the apparent major axis. The elongation tends to be associated with exponentially shaped smearing kernels and with smearing scale lengths exceeding 1 kpc. This suggests that confinement heights in the disks are on the order of 1 kpc, and smaller scale smearing corresponds to negligible escape of cosmic-ray electrons.

6. The radio-to-infrared ratio is statistically indistinguishable between galaxies with exponential smearing kernels and galaxies with Gaussian kernels. This argues in favor of the Helou & Bicay smearing model.

Subject headings: cosmic rays — galaxies: ISM — galaxies: spiral — galaxies: structure — radio continuum: galaxies

1. INTRODUCTION

In a previous paper (Marsh & Helou 1995, hereafter Paper I), we presented maps showing the spatial variation of Q_{60}, the 60 μm infrared to 20 cm radio intensity ratio, in a set of 25 nearby galaxies (24 late-type spirals and one irregular). These maps were consistent with the interpretation discussed by Bicay & Helou (1990), hereafter BH90), and developed further by Helou & Bicay (1993, hereafter HB93), in which the radio and infrared emission are strongly coupled by processes connected with the formation and subsequent evolution of massive OB stars. In this model, the infrared emission arises from dust heated by the stars, and the radio emission is synchrotron radiation from relativistic electrons accelerated during the supernova phase.

BH90 concluded that a circularly symmetric exponential function provides a good representation of the smearing function, suggesting a "leaky-box" confinement model for the electrons, as opposed to simple diffusion. Their analysis, however, contained two important simplifying assumptions:

1. The infrared brightness distribution of each galaxy was constrained to be of the form of a circularly symmetric radial exponential. Thus local structure (specifically, the localized emission peaks discussed in Paper I) was ignored.

2. The effects of disk inclination were not taken into account, and hence the analysis did not distinguish between isotropic diffusion effects and diffusion which is confined to the plane of the disk.

In this paper, we present the results of a reanalysis of the data used by BH90, without imposing either of the above constraints. Two different procedures were employed, namely, (1) a least-squares fitting procedure using assumed functional forms (exponentials and Gaussians), as described in § 4, and (2) a full deconvolution of the infrared images from the corresponding radio images, as described in § 5.

2. DATA

The galaxy sample used for this analysis was the same as for Paper I. The total number of galaxies was 25, all but one

of which are late-type spirals; the exception is IC 10, classified as an irregular.

Our input data for each galaxy consisted of images made in the infrared continuum at 60 μm wavelength and the radio continuum at 20 cm wavelength (frequency 1.49 GHz). The infrared images were made using data from the *Infrared Astronomy Satellite* (*IRAS*), using the maximum correlation method described by Aumann, Fowler, & Melnyk (1990), and have a spatial resolution somewhat better than 1'. The radio images were based on data from the Very Large Array (VLA) as presented by Condon (1987). They were subsequently processed in order to have resolution properties similar to that of the infrared images, as described in Paper I.

Since confusing point sources were apparent in many of the radio images, certain precautions were necessary in the parameter-fitting and deconvolution procedures to be described. Specifically, all radio and infrared samples which fell within a resolution element's width of the confusing sources identified by Condon (1987) were excluded from the analysis. The region surrounding the Seyfert nucleus of NGC 3031 was similarly excluded.

Although not expected to fit the smearing model, the irregular galaxy, IC 10, was included in the analysis. Since the infrared-to-radio ratio map in Paper I showed that the northwest component exhibited radial gradients while the southeast component did not, the analyzed region was confined to the northwest component.

3. MEASUREMENT MODEL

According to the smearing model, the true intensity distributions in radio and infrared are related via convolution with a smearing kernel $\kappa(r)$, where r is a two-dimensional angular position vector. In addition, the *observed* radio and infrared images [denoted by $R(r)$ and $I(r)$, respectively] are related to the true distributions via convolution with the point-spread functions (PSFs) of the respective measurement systems. Since the convolution operator is commutative, $R(r)$ and $I(r)$ would therefore be related by the same convolution kernel, $\kappa(r)$, as for the true distributions. In the absence of measurement noise and model error, we would thus have

$$R(r) = Q^{-1} \iint I(r')\kappa(r - r')d^2r' , \qquad (1)$$

where Q represents the ratio of the total flux densities in infrared and radio, assuming appropriate normalization for $\kappa(r)$.

Rewriting equation (1) in terms of quantities defined on a discrete grid of pixels and making allowance for model error, η_j, and measurement noise, v_j, the radio intensity in the jth pixel may be expressed as

$$R_j = Q^{-1}(1 + \eta_j)\Delta\Omega \sum_k I_k \kappa(r_j - r_k) + v_j , \qquad (2)$$

where $\Delta\Omega$ represents the solid angle subtended by a pixel. If we represent the model error and measurement noise by uncorrelated Gaussian random processes which are statistically independent of each other, then the model error and measurement noise terms on the right-hand side of equation (2) can be lumped into a single nonstationary noise term the local variance of which is given to a sufficiently good approximation by

$$\sigma_j^2 = \sigma_\eta^2 R_j^2 + \sigma_v^2 , \qquad (3)$$

where σ_v^2 and σ_η^2 represent the variances of measurement noise and model error, respectively.

4. PARAMETERIZED FITTING PROCEDURE

In this section we will examine the assumption that the smearing function can be represented adequately by either an exponential or a Gaussian function and will determine the set of parameters which give the best fit to the data in each case.

4.1. *Description of Technique*

We will assume that the functional form of κ can be described by the two parameters l and s, the first being a discrete-valued label representing the function type, and the second being an appropriately defined scale length. The function types which will be considered here are the following: $l = 1$, Gaussian and circular in plane of sky; $l = 2$, exponential and circular in plane of sky; $l = 3$, Gaussian and circular in the disk plane of the galaxy; and $l = 4$, exponential and circular in disk plane of the galaxy.

We will define s to be the half-width of the function at the $1/e$ points. In those cases for which the function is assumed to be circular in the disk plane, $\kappa(r)$ involves the additional parameters i and θ, representing the inclination of the disk with respect to the plane of the sky and the position of the axis of tilt, respectively.

On the basis of equation (2), maximum-likelihood estimates of l, s, and Q (denoted by $\hat{l}$, $\hat{s}$, and $\hat{Q}$, respectively) can be obtained from the observed radio and infrared images by minimizing the weighted sum of squares of residuals, given by

$$\phi(l, s, Q) = \sum_j \sigma_j^{-2}[R_j - Q^{-1}\tilde{I}_j(l, s)]^2 , \qquad (4)$$

where $\tilde{I}_j(l, s)$ represents the jth pixel of the infrared image after convolution with a kernel of functional type l and spatial scale s. For this analysis, we take σ_v as $1/70$ of the radio peak, consistent with the dynamic range of the radio images. The model-error term, σ_η, however, is unknown a priori, and therefore we estimate it from the residuals of the fit by adjusting its value until a reduced χ^2 value of unity is obtained.

The variances in the estimated values of s and Q are given by the diagonal elements of γ^{-1}, where γ is a matrix whose elements represent the second derivatives of $\phi(l, s, Q)/2$ with respect to s and Q (Kendall & Stuart 1979).

Since l is a discrete-valued quantity, its uncertainty is characterized by the relative probabilities of the possible values. Two probabilities of interest are $P_{\exp}$, which represents the probability that the optimal convolving function is an exponential rather than a Gaussian, and $P_{\rm sky}$, the probability that the optimal function is circular in the plane of the sky rather than in the plane of the galactic disk. If we assume that (1) the only possible function types are the four listed above, (2) each function is equally likely a priori, and (3) the choice between the Gaussian and exponential forms is completely independent of the choice between the sky-plane and disk-plane forms a priori, then the two probabilities are given by

$$P_{\exp} = \frac{1}{1 + \exp\left[-1/2(\phi_{\rm gauss} - \phi_{\exp})\right]} , \qquad (5)$$

$$P_{sky} = \frac{1}{1 + \exp\left[-1/2(\phi_{gal} - \phi_{sky})\right]}, \quad (6)$$

where ϕ_{exp}, ϕ_{gauss}, ϕ_{sky}, and ϕ_{gal} represent the minimum values of $\phi(l, s, Q)$ over the sets of l values {2, 4}, {1, 3}, {1, 2}, and {3, 4}, respectively. Two other probabilities related to those above are $P_{gauss} = 1 - P_{exp}$ and $P_{disk} = 1 - P_{sky}$.

The estimated statistical significance of the exponential/Gaussian and sky/disk choices represent useful figures of merit for the solutions. Another figure of merit is the rms residual of fractional model-error, η_{rms}, estimated from the residuals of the fit after subtracting the effects of known measurement noise, σ_v. To a good approximation, η_{rms} corresponds (after the σ_v correction) to the rms value of the logarithmic residual image, defined as

residual image = ln [scaled-and-convolved infrared]

$$- \ln[\text{radio}].$$

4.2. Results

The results of the parameter-estimation analysis are presented in Table 1.

An "E" or "G" in column (2) denotes that the best-fitting function was an exponential or Gaussian, respectively. The statistical significance of that identification (the larger of P_{exp} and P_{gauss}, expressed as a percentage) is given in parentheses. A "δ" in column (2) signifies that the best-fitting function was a delta-function, i.e., smoothing with exponential or Gaussian functions of significant width did not improve the correspondence between the radio and infrared images.

For the galaxies with substantial inclination to the line of sight, an "S" or "D" in column (3) denotes that the best-fitting function was circular in the sky plane or disk plane, respectively. The statistical significance is given in parentheses.

The smearing scale listed in column (4) represents the half-width at the $1/e$ points, along the major axis of the optimal smearing function. Columns (6) and (7) list, respectively, the estimated value of Q and the global flux density ratio of infrared to radio, for comparison. Finally, η_{rms}, the rms residual of fractional model error is listed in column (8).

A comparison of the estimated smearing scales with the results of BH90 reveals that the present values are systematically smaller than those of BH90, by a factor of 2 in many cases, and by 1 order of magnitude in others (NGC 55 and NGC 4631). The discrepancies most probably result from an important assumption made by BH90, but which we do not need to impose, namely a radial-exponential form of the infrared disk. Although the latter provided a good model for the inner disk, it underestimated the disk scale in the outer portions (see Fig. 5 of BH90), and, consequently, a larger smearing scale was required in order to reproduce the observed radio data. Since we use the infrared image as observed, there is no such bias present in the current estimates.

In order to investigate possible differences in the behavior of the estimated quantities as a function of position in the galaxy, the above analysis was repeated for the inner and outer regions of each galaxy. No significant difference was found between the estimated smearing scales for the two regions.

The probabilities given in Table 1 provide an objective basis for drawing conclusions as to the form of the smearing function. In the absence of a signal P_{exp} and P_{sky} would be precisely 50%; larger values imply increased distinguishability of different models in the presence of the noise. If we arbitrarily take 90% as our confidence criterion, then 11 of

TABLE 1
PARAMETER ESTIMATION AND DECONVOLUTION RESULTS

GALAXY (1)	FUNCTION TYPE		SMEARING SCALE (kpc)		Q		RMS RESIDUALS	
	E/G (2)	S/D (3)	Fitted (4)	Deconvolved (5)	Fitted (6)	Flux Ratio (7)	Fitted (8)	Deconvolved (9)
IC 10............	E(59)	...	0.16 ± 0.07	0.14 ± 0.07	408 ± 20	356	0.14	0.17
NGC 55	E(54)	S(96)	0.16 ± 0.02	0.32 ± 0.18	217 ± 5	200	0.10	0.11
NGC 253	E(53)	D(76)	0.29 ± 0.09	0.54 ± 0.16	212 ± 9	175	0.42	0.54
NGC 628	δ	...	<0.5	...	292 ± 14	219	...	...
NGC 891	G(56)	S(66)	0.89 ± 0.08	2.27 ± 0.50	91 ± 1	91	<0.01	<0.01
NGC 1097......	G(54)	S(66)	1.56 ± 0.12	3.05 ± 1.09	128 ± 1	117	<0.01	<0.01
NGC 1569......	G(77)	S(100)	0.19 ± 0.01	0.32 ± 0.14	119 ± 1	118	<0.01	<0.01
NGC 2403......	G(53)	S(52)	0.36 ± 0.05	0.45 ± 0.14	269 ± 2	257	0.12	0.10
NGC 2903......	G(74)	S(100)	1.19 ± 0.3	1.93 ± 0.20	136 ± 1	137	<0.01	<0.01
NGC 3031......	G(51)	S(64)	0.33 ± 0.10	0.23 ± 0.23	250 ± 3	148	0.57	0.57
NGC 3344......	E(53)	...	0.96 ± 0.13	0.59 ± 0.59	131 ± 4	129	0.09	0.14
NGC 3556......	E(86)	D(100)	2.37 ± 0.28	2.34 ± 0.50	112 ± 4	110	<0.01	0.06
NGC 3621......	E(95)	D(94)	1.79 ± 0.18	2.71 ± 0.12	133 ± 4	132	<0.01	<0.01
NGC 4254......	G(54)	...	2.54 ± 0.43	2.30 ± 1.16	86 ± 1	82	0.19	0.43
NGC 4303......	G(60)	...	3.56 ± 0.41	2.76 ± 0.85	182 ± 3	146	0.43	0.33
NGC 4490......	E(84)	D(100)	1.04 ± 0.07	2.30 ± 0.27	60 ± 1	60	<0.01	<0.01
NGC 4565......	G(59)	D(68)	3.43 ± 1.22	5.57 ± 0.42	108 ± 2	88	0.16	0.18
NGC 4631......	E(58)	S(90)	0.63 ± 0.08	1.32 ± 0.59	72 ± 2	73	0.13	0.14
NGC 5055......	G(55)	S(85)	1.37 ± 0.11	1.59 ± 0.35	124 ± 1	123	<0.01	<0.01
NGC 5194......	E(93)	...	1.90 ± 0.34	1.36 ± 0.42	95 ± 3	85	0.16	0.18
NGC 5236......	E(97)	...	1.07 ± 0.28	0.74 ± 0.35	126 ± 4	116	0.06	0.06
NGC 5907......	δ	...	<0.1	...	172 ± 5	158	...	...
NGC 6946......	E(99)	...	0.78 ± 0.10	0.70 ± 0.36	99 ± 2	97	0.13	0.16
NGC 7331......	G(62)	D(99)	3.88 ± 0.41	4.66 ± 0.47	98 ± 1	90	0.08	0.08
NGC 7793......	G(52)	S(51)	0.36 ± 0.11	0.47 ± 0.20	247 ± 3	213	0.30	0.29

Galaxy	Sky/Disk	Smearing Scale (kpc)
NGC 55	Sky (96)	0.16 ± 0.02
NGC 1569	Sky (100)	0.19 ± 0.01
NGC 4631	Sky (90)	0.63 ± 0.08
NGC 4490	Disk (100)	1.04 ± 0.07
NGC 2903	Sky (100)	1.19 ± 0.03
NGC 3621	Disk (94)	1.79 ± 0.18
NGC 3556	Disk (100)	2.37 ± 0.28
NGC 7331	Disk (99)	3.88 ± 0.41

[a] For solutions with greater than 90% significance.

the 25 galaxies gave statistically significant results with regard to the choice of smearing function. The galaxies with greater than 90% confidence in the exponential/Gaussian choice were NGC 3621, NGC 5194, 5236, and 6946; those with greater than 90% confidence in the sky/disk choice are listed in Table 2. The galaxies in Table 2 are listed in order of increasing smearing scale, from which it is apparent that for galaxies whose smearing scale is less than 1 kpc, the smearing function tends to be circular in the plane of the sky, whereas for scales greater than 1 kpc it tends to be circular in the disk plane of the galaxy (i.e., elongated when projected on the plane of the sky). This will be discussed further in § 6.
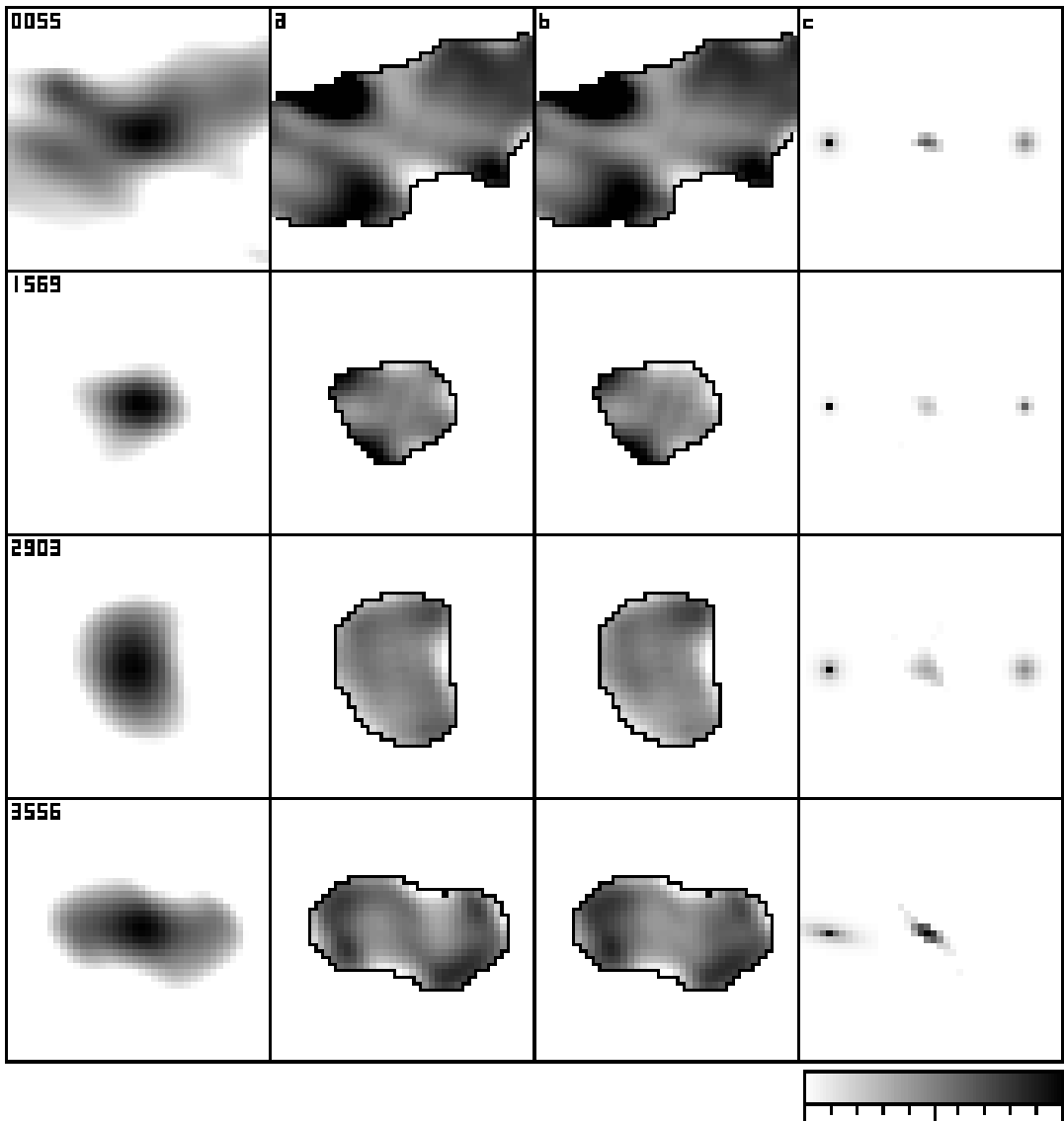

FIG. 1a

FIG. 1.—(a)–(c) Residual maps and estimated kernels, presented with the radio images for comparison, with a field of view of 15′ × 15′ in each case. The left-hand plot in each case shows the 20 cm radio image on a logarithmic scale of 2 decades; the plots in column (a) show the residuals of the fit of the radio data after the parameter-fitting procedure, and those in the (b) column show the residuals after deconvolution. The residuals are defined as

$$\ln [\text{scaled-and-convolved infrared}] - \ln [\text{radio}]$$

and are plotted with a range of −1.0 to +1.0 in each case, such that black is positive and white is negative.

The estimated smearing kernels are shown on a linear scale in column (c). The central kernel represents the results of deconvolution, while the left and right kernels represent the best-fit exponential and Gaussian functions, respectively, for comparison. The omission of the best-fit Gaussians for four of the galaxies is due to the fact that in these cases, no Gaussian of significant width gave any improvement over a delta function.
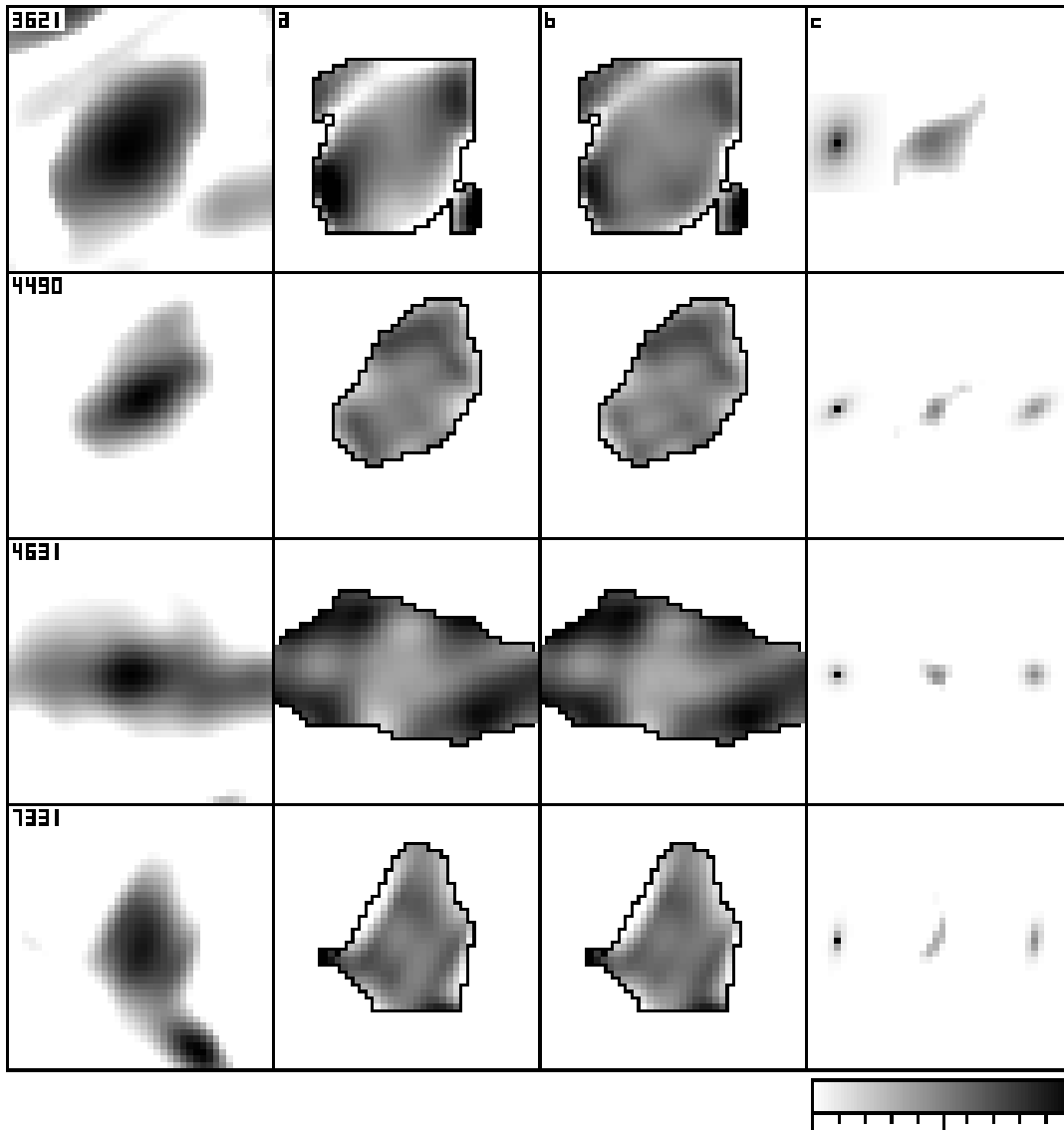
FIG. 1b

The logarithmic residuals of the fit for each of the above 11 galaxies are shown in column (*a*) in Figure 1, alongside the corresponding radio image. In order to determine whether these residuals could be improved by using some other choice of smearing function, we have estimated the latter by direct deconvolution, and the results are described in the next section.

5. DECONVOLUTION PROCEDURE

Since equation (1) is a convolutional relation, the function $\kappa(r)$ can, in principle, be estimated by deconvolving the observed infrared image from the corresponding radio image. Since deconvolution is a noise-vulnerable process, however, it must be carried out within the framework of an estimation procedure in which the data are properly weighted with regard to measurement variance. In addition, the spatial resolution of the results can be improved by imposing a nonnegativity constraint with respect to the pixel values of the estimated kernel. A suitable algorithm has been described by Richardson & Marsh (1983) and applied to astronomical image deconvolution by Marsh et al. (1995). In applying this algorithm, we have used the same noise model as used in the parameter estimation procedure, in which the variance of additive noise is given by equation (3), taking the local model error (i.e., σ_η) at the nominal value of 10%.

In order to assess the spatial resolution of each estimated smearing kernel, each of the radio images was deconvolved from itself. It was found that the central peaks of the resulting images had dimensions (defined by the FWHM along minor and major axes) typically of 2×3 pixels, and hence the deconvolved smearing kernels have a resolution of this order. This translates into an uncertainty in deconvolved size, as listed in Table 1.

5.1. Results

The results of the deconvolution (estimated smearing scale and the rms residual model error) are presented in columns (5) and (9) of Table 1, alongside the parameter-estimation results for comparison. In addition, for the 11 galaxies which gave significant parameter fits, the images from the deconvolution analysis (residual images and esti-
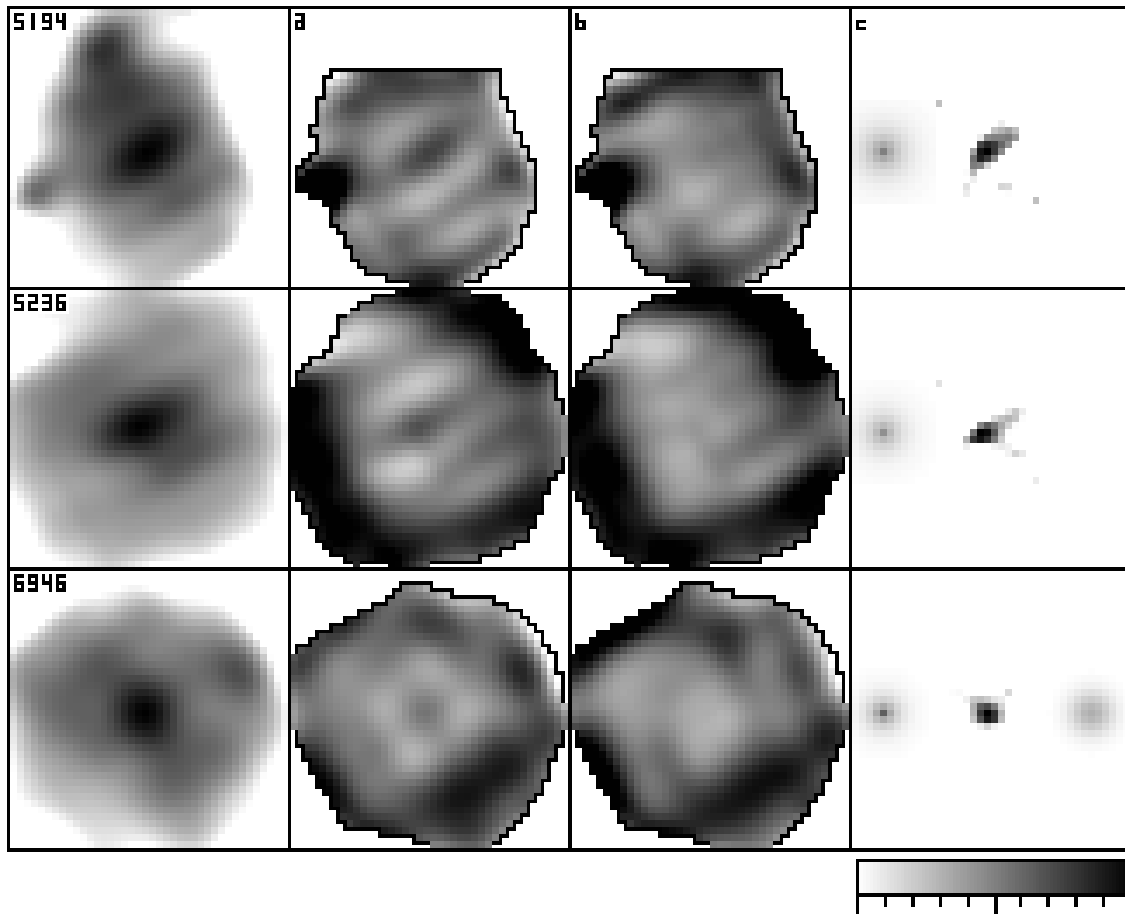
FIG. 1c

mated kernels) are presented in columns (*b*) and (*c*), respectively, in Figure 1. For each galaxy (except as noted in the caption), three kernel images are shown: the center kernel represents the result of deconvolution; this is flanked by the best-fit exponential (*left*) and best-fit Gaussian (*right*) from the analysis of § 4.

Comparison of the smearing scales in columns (4) and (5) of Table 1 shows that the deconvolved values correlate well with the parameter estimates, although the former are systematically larger than the latter because of the finite resolution of the deconvolution procedure.

It is also apparent, both from the rms residuals in Table 1 and from the residual images in Figure 1, that deconvolution has not significantly improved the quality of the fit beyond that obtained from parameter estimation. The fact that the residuals from deconvolution are actually worse in some cases is a result of the fact that the response outside of the central region (15 × 15 pixels) of the deconvolved kernel was ignored.

In order to look for evidence of *radial* anisotropy (i.e., that the smearing has a preferred direction with respect to the galactic center), the deconvolution analysis was repeated using subsets of the data, selected on the basis of azimuthal location. Specifically, the radio image for each galaxy was divided into four quadrants centered on the position of the central peak and delineated by the north-south and east-west axes in the sky. The smearing function was then estimated separately for each quadrant and compared with the reference function (obtained by decon-

volving the radio image from itself) in order to assess whether any quadrant-dependent differences were significant. No evidence for any radial anisotropy was found at a resolution of 1′.

6. DISCUSSION

The results of the analyses described in §§ 4 and 5 show that the radio images can be reproduced, to reasonable accuracy, by smearing the infrared images with relatively compact, positive-valued kernels. In most cases, the residuals are ≲10% in radio intensity, over an intensity range of almost 2 orders of magnitude. Furthermore, the simple, single-peaked morphology of the estimated smearing kernels is consistent with a process dominated by diffusion.

On the question of the best form of the convolving function, we find the following:

1. Table 1 shows that the preference for an exponential is significant ($P_{exp} > 0.9$) for four of the 25 galaxies, whereas there is *no* significant preference for a Gaussian form in *any* of the remaining cases. There are two galaxies with $P_{gauss} \sim 0.75$ and all others have $P_{gauss} \leq 0.6$.

2. Table 2 also shows that in some cases, the best-fit function is circular in the plane of the sky, while in others it is circular in the plane of the galactic disk, i.e., is elongated like the appearance of the galaxy as projected onto the plane of the sky.

3. In all but one of the cases for which the smearing

function is circular in the plane of the sky, the smearing scale is less than 1 kpc. Conversely, in all cases for which the smearing function is elongated along with the galaxy, the smearing scale is greater than 1 kpc. At first glance, this migh seem like a resolution effect, whereby the smearing kernels of the most distant galaxies are spatially unresolved and therefore circular in the plane of the sky. If this were the case, however, the delineation between elongated and non-elongated galaxies would occur at a fixed angular scale rather than linear scale (a significant distinction in view of the fact that the subset of inclined galaxies spans 1 order of magnitude in distance, namely, 2.9–25.7 Mpc; BH90). Furthermore the two galaxies with the strongest preferences for a function which is circular in the sky plane (NGC 55 and NGC 1569) also happen to be the two closest galaxies in the subset (3.2 and 2.9 Mpc, respectively). At such distances, elongation on scales ~ 1 kpc would have been easily detectable if present. This argues strongly for a noninstrumental origin for the effect.

6.1. *Comparison to Models*

The median smearing length for the galaxies studied is 1.04 kpc; nearly one-third of the sample galaxies (seven objects) have a smearing scale length between 0.6 and 1.2 kpc. The latter interval maps roughly to a range of 1–10 cm^{-3} in mean interstellar densities, using Figure 2 in HB93, which assumes $h_0 = 100$ pc, $B \propto n^{1/2}$, and $l_{mfp} = 1$ pc $[n/(cm^{-3})]^{-1/3}$ for 10 GeV electrons. For these assumptions, the range of scale lengths observed marks the transition from cosmic-ray electron (CRE) losses being dominated by escape to being dominated by synchrotron decay. Under the same assumptions, the smallest observed smearing lengths at less than 0.5 kpc imply yet higher mean interstellar densities in the galaxy.

The observation that smearing kernels become elongated in the galaxy disk only once their scales exceed about 1 kpc suggests that this height is typical of the scale heights of disks. If disk scale heights are indeed closer to 1 kpc than 100 pc, then we must reexamine the validity of our density estimate above. In this regard we note that, since the scale height, h_0, used in Figure 2 of HB93 describes the dust associated with interstellar gas rather than the radio disk thickness which we infer here, the density estimates remain valid, subject to the caveats expressed in that paper. The larger scale heights do, however, affect the parameters of the simple confinement model sketched out in § 5 of HB93. In this model, the product $h_0^{-1} \times \epsilon_{esc}^{1/2}$ was required to be constant, with the escape probability of a cosmic ray at each visit to the disk boundary $\epsilon_{esc} \lesssim 10^{-3}$ for $h_0 = 100$ pc. If h_0 were increased to 1 kpc the escape probability would also have to be increased to roughly 0.1, probably a more reasonable confinement efficiency given the weak and fragmented magnetic field one would expect high above a galactic disk.

The distributions of the infrared-to-radio ratio, Q, for exponentially smeared and Gaussian smeared galaxies are statistically indistinguishable. This might seem surprising at first glance because CRE losses by escape should dominate in the first group while losses by synchrotron decay should dominate in the second one. This would seem to suggest that systems with escaping CRE would have larger Q values. However, this is not necessarily the case, for galaxies that retain poorly their CRE may also let more of the heat

photons escape. In fact, the HB93 model is especially attractive because it offers a natural explanation for the constancy of Q against changing CRE escape fraction, by relating it directly to effective optical depth in the galaxy.

6.2. *Variation in Convolution Kernel*

The fact that, in many cases, significant residuals remain even after the use of the optimal smearing function (estimated by deconvolution) indicates that the relation between the infrared and radio continuum images of a galaxy is more complex than could be described by a simple smearing model. This complexity could arise in several ways, the simplest of which is that while the radio continuum is a smeared version of the infrared, the smearing kernel varies its size, shape, or both as a function of location within the galaxy.

The quadrant analysis in § 5.2 rules out one limited case of shape variation, namely, that the kernel might be elongated in the radial direction in the galaxy. Such an anisotropy is physically plausible given the strong radial density gradients in galaxy disks, yet it is not observed. The same density gradient suggests as equally plausible a radial gradient in the size of the smearing kernel. This too is ruled out, however, by the results of the comparison of inner with outer disk regions in § 4.2. Apart from systematic variations, the scale length of the smearing kernel is also sensitive to the age of the cloud of CRE responsible for the synchrotron emission, and to the local magnetic field strength and geometry, all of which are known to vary in galactic disks (Krause 1990). This random variation may well be the main contributor to the residual discrepancies between the radio image and the smeared infrared image and may in addition obscure any systematic trends across the disk.

6.3. *Other Process*

Another possibility to explain the residuals in the comparison between the radio and smeared infrared is that "smearing" by convolution is an incomplete description of the relation between the two images. This would imply that spreading, decay, and escape are not the dominant processes for radio-emitting CRE or that CRE sources are not coincident with massive stars. The latter hypothesis is refuted by the excellent correlation between global infrared and radio luminosities, so we will consider only the acceleration of CRE far from their original sources. The results of Paper I, especially that Q peaks only at the intensity peaks, argue that reacceleration cannot be a dominant process but do not rule it out entirely. If reacceleration is due to diffuse shocks in the interstellar medium (Duric 1988), then the relation between infrared and radio might still be amenable to description by a convolution, albeit with a flat-topped or, at most, centrally depressed kernel. We therefore conclude that if reacceleration is the cause of the residuals under discussion, it is more likely to be linked to localized features such as spiral density waves or supernova shocks, as this would lead to more variation in the radio emission profiles around cosmic ray sources.

Another possibility is that a significant fraction of CRE escape through breaches in the disk associated with superbubbles or other accidents (Rand & van der Hulst 1993), rather than in a distributed, steady state mode. The convolution description would be rendered inadequate by sudden partial escapes at random locations.

7. SUMMARY

We have presented quantitative tests of the "smearing" model (HB93) for relating radio and infrared images of spiral galaxies. In this model, the infrared emission is stellar luminosity reprocessed by dust, whereas radio emission is produced by synchrotron emission from relativistic particles accelerated by supernovae. Since these electrons continue to radiate as they diffuse, the radio image appears as a smeared version of the infrared image. We have tested the model on a set of 24 spirals and one irregular, using 20 cm radio images and 60 μm infrared images processed to the same resolution of $\simeq 1'$. The BH90 study, which assumed circularly symmetric and exponentially profiled disks, had suggested that the smearing function is best approximated to have an exponential radial profile. We present here a detailed assessment of the shape and size of the smearing function free of the above assumptions. We used two different approaches: (1) parameterized fits to exponential and Gaussian functions, each either circularly symmetric or elongated along the disk's apparent major axis, and (2) direct estimation of the form of the kernel by deconvolution of the radio image against the infrared image. We conclude that the following:

1. The radio images are indeed reproduced to reasonable accuracy by smearing the infrared images with positive-valued kernels, with model-error residuals $\leq 10\%$ of the local radio intensity over an intensity range of almost 2 orders of magnitude.

2. Most estimated smearing scales are smaller than 2 kpc, with a median of about 1 kpc. They are typically 50% smaller than those reported by BH90. This discrepancy is most likely due to the specific infrared intensity distribution assumed by BH90.

3. The discrimination between exponential and Gaussian smearing kernels is marginal in most cases: above the 90% confidence level, only four galaxies are better fit by an exponential kernel, and none is better fit by a Gaussian. There is also no improvement in the goodness of fit if we use direct deconvolution rather than parametric Gaussian or exponential fitting.

4. There is no evidence for a change of shape of the smearing kernel from one quadrant of the galaxy disk to another. The smearing is therefore unlikely to be elongated in the radial direction.

5. For some but not all galaxies inclined to the line of sight by 45° or more, the smearing function is significantly elongated parallel to the apparent major axis. The elongation tends to be associated with exponentially shaped smearing kernels and with smearing scale lengths exceeding 1 kpc. Gaussian-shaped kernels tend toward shorter scale lengths and no elongation. This suggests that confinement heights in the disks are on the order of 1 kpc, and smaller scale smearing corresponds to negligible escape of cosmic-ray electrons.

6. The radio-to-infrared ratio is statistically indistinguishable between galaxies with exponential smearing kernels and galaxies with Gaussian kernels. This argues in favor of the HB93 smearing model, which offers a natural explanation for the constancy of Q against changing CRE escape fraction, by relating it directly to effective optical depth in the galaxy.

REFERENCES

Aumann, H. H., Fowler, J. W., & Melnyk, M. 1990, AJ, 99, 1674
Bicay, M. D., & Helou, G. 1990, ApJ, 362, 59 (BH90)
Condon, J. J. 1987, ApJS, 65, 485
Duric, N. 1988, Space Sci. Rev., 48, 73
Helou, G., & Bicay, M. D. B. 1993, ApJ, 415, 93 (HB93)
Kendall, M., & Stuart, A. 1979, The Advanced Theory of Statistics, Vol. 2, Infererence and Relationship (London: Charles Griffin)
Krause, M. 1990, in Galactic and Intergalactic Magnetic Fields, ed. R. Beck, P. P. Kronberg, & R. Wielebinski (Dordrecht: Kluwer), 187
Marsh, K. A., & Helou, G. 1995, ApJ, 445, 599 (Paper I)
Marsh, K. A., Van Cleve, J. E., Mahoney, M. J., Hayward, T. L., & Houck, J. R. 1995, ApJ, 451, 777
Rand, R. J., & van der Hulst, J. M. 1993, AJ, 105, 2098
Richardson, J. M., & Marsh, K. A. 1983, Proc. SPIE, 413, 79